

# Hybrid analytical model of switched reluctance machine for real-time hardware-in-the-loop simulation

Fengqiu Xu<sup>1,2</sup> ✉, Venkata Dinavahi<sup>2</sup>, Xianze Xu<sup>1</sup>

<sup>1</sup>Electrical Information School, Wuhan University, Luojia Shan, Wuhan, Hubei Province, People's Republic of China

<sup>2</sup>Department of Electrical and Computer Engineering, University of Alberta, 9107-116 st., Edmonton T6G 2V4, Alberta, Canada, T6G2V4

✉ E-mail: hncxu@whu.edu.cn

ISSN 1751-8660

Received on 15th December 2016

Revised on 14th February 2017

Accepted on 6th March 2017

doi: 10.1049/iet-epa.2016.0831

www.ietdl.org

**Abstract:** Applications of switched reluctance machine (SRM) are increasing in the industry due to their many desirable features. This study proposes a hybrid analytical model (HAM) of the SRM for the hardware-in-the-loop (HIL) simulation. To obtain satisfactory accuracy, the phase flux linkage is solved by the magnetic equivalent circuit (MEC) method when the stator and rotor poles overlap, and by the space harmonic method (SHM) when the poles do not overlap. The backward Euler and Newton–Raphson methods are used to calculate the exciting current, while the Gaussian quadrature is used to compute the electromagnetic torque in the HIL simulation. The digital hardware implementation of computation components are developed on the field-programmable gate array by exploiting the parallel hardware architecture and fully pipelined arithmetic processing. To highlight the performance of the HAM, the captured real-time results are compared with the off-line transient solution obtained through the co-simulation of Ansys Maxwell<sup>®</sup>, Ansys Simplorer<sup>®</sup>, and Simulink<sup>®</sup>, which model the SRM, drive circuit, and control system, respectively.

## Nomenclature

$\theta$	mechanical rotation of rotor
$\theta_r$	rotor position respect to one phase of stator
$\theta_c$	cycle of rotor position
$\theta_m$	threshold $\theta_r$ between non-overlap and overlap
$\varphi_1, \varphi_2$	represent the range of current region in SHM
$\lambda$	flux linked by one phase in the stator
$\lambda_s$	flux linkage solved by SHM
$\lambda_e$	flux linkage solved by MEC
$\lambda_m, \lambda_f$	main and fringing flux linkage of $\lambda_e$
$\mu_0$	permeability of vacuum
$\mu_r$	relative permeability of iron
$D_r, D_s$	diameter of rotor and stator
$D_{ry}, D_{sy}$	diameter of rotor yoke and stator yoke
$l_{stk}$	the thickness of stator and rotor
$\beta_r, \beta_s$	radian of rotor pole and stator pole
$N, M$	turns of the coils, phase number of SRM
$s$	switch states of IGBT inverter
$I_h, I_n$	history and new exciting current of phase coils
$t_s$	time-step in HIL simulation
$T_e$	electromagnetic torque of SRM
$J, \eta$	moment of inertia and damping of rotor
$\omega_h, \omega_n$	history and new angular speed of rotor
$\theta_h, \theta_n$	history and new rotation of rotor

## 1 Introduction

The switched reluctance machine (SRM) is anticipated to be used in a growing number of applications due to its inherent simple construction, low inertia, high torque-weight ratio, easy speed control, and strong fault tolerance. Plenty of studies about the controller, driver, and optimisation of the SRM have been reported [1–6]. Before these developments were employed in reality, off-line simulation was always employed to verify the performance of the control system. However, the designed controller could not be tested in the real plant, which resulted in unpredictable issues occurring in the subsequent commissioning. In such a case, hardware-in-the-loop (HIL) simulation is a reliable and

cost-effective alternative in virtual scenarios for testing real devices in the design of the SRM drive systems [7–9]. Currently, HIL simulation is widely applied for investigating the real-time behaviour of the control system. Interfaced with the emulator, the real controller is able to control the virtual objects, and we can adjust the design parameter of the controller via analysing the outputs of the real-time model. A detailed, accurate, and efficient system or plant model is the prime requirement in the HIL simulation to reproduce the realistic behaviour of tested controller. On the premise of real-time computation, the solution of the proposed model for SRM should be sufficiently accurate enough.

The characteristics of the SRM can be described as the magnetic flux linked by the phase on the stator with respect to different rotor positions and exciting current. In the literature, there are various methods to obtain the flux linkage:

- (i) geometry-based analytical model [10–14];
- (ii) finite element method (FEM) [15–17];
- (iii) space harmonic method (SHM) [18–20];
- (iv) magnetic equivalent circuit (MEC) method [21–23].

Using measurements or the results from detailed FEM simulation, the geometry-based analytical model curve fits the phase flux linkage as a product of two non-linear equations for current and rotor position, respectively, based on the space periodicity of the SRM. This procedure is employed by many off-line simulations such as in Simulink<sup>®</sup>; however, the main drawback is that the characteristics of the SRM must be obtained in advance and significant error can occur if the operation state is different from the pre-defined state used to construct the model. FEM offers excellent detail and accuracy, however it is time-consuming and cannot meet the strict execution time constraint of HIL simulation. In the SHM, the flux linkage is obtained via the solution of the magnetostatic Maxwell's equation, but the method is unavailable when the stator pole and rotor pole overlap because the stator and rotor iron suffer from severe magnetic saturation. MEC method is an alternative for modelling the SRM with reasonable computational effort; however, this method is inaccurate when the rotor locates in the non-overlapping range because the flux path cannot be estimated exactly. The last two methods are effective in

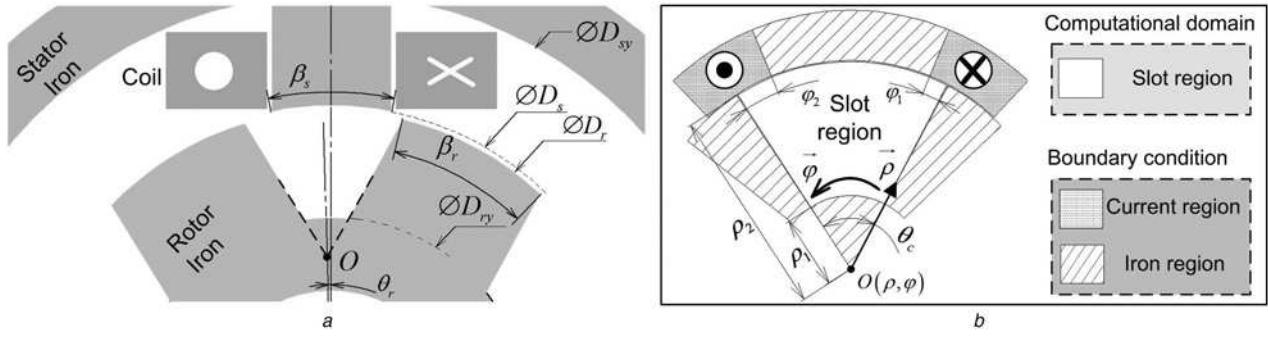


**Fig. 1** Schematic of SRM with rotor and stator poles non-overlapping  
a Schematic of rotor and stator poles  
b Schematic of SHM to compute the flux linked by a phase

different stroke of the machine; therefore, a hybrid analytical model (HAM) is proposed in this paper utilising the SHM in the range with no rotor stator pole overlap and MEC in the range with rotor stator pole overlap, respectively.

In the proposed model, the non-linear characteristics of the SRM can be calculated accurately. However, there still exists the certain computational burden. Thanks to the dramatic developments in the very large-scale integration technologies, the field-programmable gate array (FPGA), which possesses inherent parallel architecture and provides the nanosecond computational clock cycle, has become an advanced computational engine for digital hardware realisation of the electrical machines [24, 25]. Taking advantage of IP cores of trigonometric and floating-point math functions, the HAM is implemented on FPGA through VHDL language and realises 5  $\mu$ s time-step for the HIL emulation with a 100 MHz FPGA clock.

The rest of the paper is organised as follows. Section 2 introduces the HAM and constructs the relative circuit and dynamic equations to describe the operation of the SRM drive system. The FPGA-based real-time hardware for realising these associated non-linear equations are presented in Section 3. In Section 4, the steady-state characteristics of an 8/6 SRM and a 6/4 SRM solved by the proposed HAM are compared with the result from FEM software. In addition, the closed-loop controller are used in the HIL simulation and the results are compared against the solution obtained by co-simulation of Ansys Maxwell<sup>®</sup>, Simplorer<sup>®</sup> and Matlab/Simulink<sup>®</sup>. Section 5 gives the conclusions of this study.

## 2 Non-linear modelling of SRM drive system

The HAM used to solve the phase flux linkage is the foundation of the HIL simulation for the SRM drive system, because both the exciting current in the SRM drive and the electromagnetic torque in the motor dynamics are dependent on the magnetic flux linked by each phase.

### 2.1 HAM of SRM

In the HAM, the two analytical models are derived for two different ranges of rotor position depending on  $\theta_r$ , as the MEC and the SHM are employed with or without rotor stator pole overlap, respectively. In addition,  $\theta_r$  is obtained via the modulus operation returning the remainder after division of  $\theta$  by  $\theta_c$ , and is equal to 0 at the most unaligned position.

**2.1.1 Flux linkage at non-overlapping position:** When the stator and rotor are non-overlapping as shown in Fig. 1a, solving the vector potential in the rotor slot is a typical 2D field problem as described in [18]. The solution in that work is derived in Cartesian coordinates, and the result cannot be convergent when  $\theta_r$  is equal to  $\theta_m$ . In this study, the flux is solved in polar coordinates to retain the geometric features of SRM, and essentially, a

convergent solution can be obtained. As shown in Fig. 1b, a 2D polar coordinate system  $O(\rho, \varphi)$  is built, in which the origin  $O$  is the intersection of two sidelines of rotor poles, and the vector  $\rho$ , coincided with one sideline, is the polar radius whose argument is zero. The rotor slot can be considered as a fan-shaped section approximately, and the outer radius  $\rho_2$  and inner radius  $\rho_1$  are given as

$$\rho_2 = \frac{D_r}{2} \cdot \sin\left(\frac{\theta_c}{2} - \frac{\beta_r}{2}\right) \div \sin\left(\frac{\theta_c}{2}\right), \quad (1)$$

$$\rho_1 = \rho_2 - \left(\frac{D_r}{2} - \frac{D_{ry}}{2}\right), \quad (2)$$

where  $\theta_c$  is equal to  $\pi/3$  or  $\pi/2$  in the 8/6 SRM or 6/4 SRM respectively. Defined in the polar coordinate system  $O(\rho, \varphi)$ ,  $\varphi_1$  and  $\varphi_2$  in the Fig. 1b are solved by

$$\varphi_1 = \frac{\theta_c}{2} - \arcsin \frac{D_s \cdot \sin((\beta_s/2) + \theta_r)}{\sqrt{D_s^2 + 4d^2 - 4D_s d \cdot \cos((\beta_s/2) + \theta_r)}}, \quad (3)$$

$$\varphi_2 = \frac{\theta_c}{2} - \arcsin \frac{D_s \cdot \sin((\beta_s/2) - \theta_r)}{\sqrt{D_s^2 + 4d^2 - 4D_s d \cdot \cos((\beta_s/2) - \theta_r)}}, \quad (4)$$

where  $d$  represents the distance between the origin  $O$  and the axial of motor

$$d = \frac{D_r}{2} \sin \frac{\theta_c - \beta_r}{2} \left( \cot \frac{\theta_c - \beta_r}{2} - \cot \frac{\theta_c}{2} \right). \quad (5)$$

Combining the vector potential  $A$  and current density  $J$  with the magnetostatic Maxwell's equations gives

$$\nabla^2 A = -\mu J. \quad (6)$$

Since the current flows in the  $z$  direction, only the  $z$  component of the vector potential is non-zero, and there is no current in the rotor slot, hence (6) reduces to Laplace's equation

$$\nabla^2 A_z = 0. \quad (7)$$

If there is no rotor and stator pole overlap, the air gap is large enough so that the magnetic saturation can be ignored in the iron. Thus, the permeability of the iron is approximated as infinite and the field in the iron is taken to be zero. In this case, the boundary condition on the boundary of the section where iron exists is that the tangential component of  $H$  field is zero

$$H_\rho|_{\varphi=0} = 0, \quad H_\rho|_{\varphi=\theta_c} = 0, \quad H_\varphi|_{\rho=\rho_1} = 0. \quad (8)$$

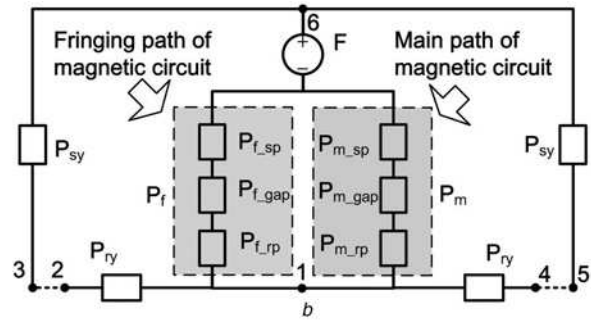
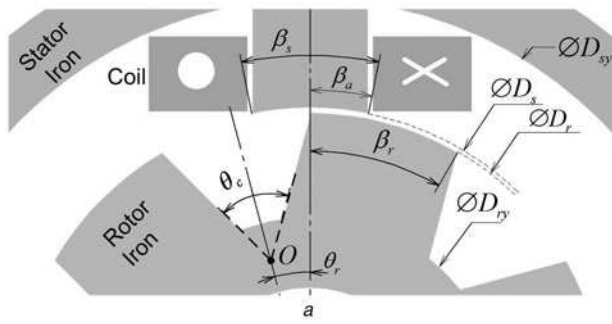


**Fig. 2** Schematic of SRM with rotor and stator poles overlapping

a Schematic of rotor and stator poles  
b Schematic of MEC model to compute the flux linked by a phase

The  $H$  field at the upper boundary of the section is also zero in the region where the stator pole locates, and is approximate to a constant where no iron exists. The constant can be solved by Ampere's law and concluded as

$$\begin{cases} H_{\varphi}|_{\rho=\rho_2} = \frac{NI}{\rho_2 \cdot \varphi_1}, & 0 \leq \varphi \leq \varphi_1 \\ H_{\varphi}|_{\rho=\rho_2} = 0, & \varphi_1 < \varphi < \theta_c - \varphi_2, \\ H_{\varphi}|_{\rho=\rho_2} = -\frac{NI}{\rho_2 \cdot \varphi_2}, & \theta_c - \varphi_2 \leq \varphi \leq \theta_c \end{cases} \quad (9)$$

and expanded as a Fourier series

$$H_{\varphi} = \sum_{n=1}^{\infty} a_n \cdot \cos\left(\frac{n\pi}{\theta_c} \varphi\right), \quad (10)$$

where  $a_n$  is calculated by

$$a_n = -\frac{2NI}{\pi n} \left\{ \frac{\sin(n\pi\varphi_1/\theta_c)}{\varphi_1 \cdot \rho_2} + \frac{\sin(n\pi(\theta_c - \varphi_2)/\theta_c)}{\varphi_2 \cdot \rho_2} \right\}. \quad (11)$$

The segregation variable method is used to solve (7).  $A_z(\rho, \varphi)$  can be written as

$$A_z(\rho, \varphi) = P(\rho) \cdot \Phi(\varphi), \quad (12)$$

hence  $P(\rho)$  and  $\Phi(\varphi)$  meet the equations of

$$\begin{cases} \rho^2 \cdot P''(\rho) + \rho \cdot P'(\rho) - m \cdot P(\rho) = 0 \\ \Phi''(\varphi) + m \cdot \Phi(\varphi) = 0 \end{cases} \quad (13)$$

Compared with the boundary condition given in (8) and (9), the solution of Laplace's equation inside the rotor slot is given as

$$A_z(\rho, \varphi) = \sum_{n=1}^{\infty} (B_n \cdot \rho^{n\pi/\theta_c} + C_n \cdot \rho^{-(n\pi/\theta_c)}) \cos\left(\frac{n\pi}{\theta_c} \varphi\right). \quad (14)$$

The  $H_{\varphi}$  field where  $\rho = \rho_1$  and  $\rho = \rho_2$ , is found by taking the curl of the vector potential and dividing by vacuum permeability  $\mu_0$ . Combined with the boundary condition,  $B_n$  and  $C_n$  are solved as

$$\begin{cases} B_n \cdot \rho_1^{(n\pi/\theta_c)-1} - C_n \cdot \rho_1^{-(n\pi/\theta_c)-1} = 0 \\ B_n \cdot \rho_2^{(n\pi/\theta_c)-1} - C_n \cdot \rho_2^{-(n\pi/\theta_c)-1} = a_n \cdot \mu_0 \cdot \frac{\theta_c}{n\pi} \end{cases} \quad (15)$$

and the solution of  $B_n$  and  $C_n$  are

$$\begin{cases} B_n = \frac{a_n \cdot \mu_0 \cdot \theta_c \cdot \rho_2}{n\pi \left( \rho_2^{n\pi/\theta_c} - \rho_1^{-2n\pi/\theta_c} \cdot \rho_2^{-n\pi/\theta_c} \right)} \\ C_n = \frac{a_n \cdot \mu_0 \cdot \theta_c \cdot \rho_2}{n\pi \left( \rho_1^{-2n\pi/\theta_c} \cdot \rho_2^{n\pi/\theta_c} - \rho_2^{-n\pi/\theta_c} \right)} \end{cases} \quad (16)$$

Substituting (16) into (14) to obtain the final solution for the vector potential  $A_z(\rho, \varphi)$ , we get

$$A_z(\rho, \varphi) = \sum_{n=1}^{\infty} \frac{a_n \theta_c \rho_2}{n\pi} \cdot \cos\left(\frac{n\pi}{\theta_c} \varphi\right) \cdot \frac{\rho^{n\pi/\theta_c} + \rho_1^{2n\pi/\theta_c} \cdot \rho^{-(n\pi/\theta_c)}}{\rho_2^{n\pi/\theta_c} - \rho_1^{-2n\pi/\theta_c} \cdot \rho_2^{-n\pi/\theta_c}}. \quad (17)$$

Based on Stokes' theorem, the flux linked by one phase around the stator pole is given as: (see (18))

**2.1.2 Flux linkage at overlapping position:** When the stator and rotor are overlapping as shown in Fig. 2a, the phase flux linkage can be solved via MEC. Fig. 2b presents the magnetic circuit of one winding in a phase, in which the circuit is divided into main path and fringing path whose permeance are  $P_m$  and  $P_f$  respectively. In addition,  $F$ , equals to  $NI$ , is the magnetic motive force (MMF),  $P_{sy}$  and  $P_{ry}$  represent the permeance of stator yoke and rotor yoke, respectively. Since each phase of SRM contains two symmetric windings, the scalar magnetic potential of nodes 2 and 3 in Fig. 2b are equal, and the same as nodes 4 and 5. We can assume the  $P_{sy}$  and  $P_{ry}$  are infinite because the magnetic saturation of stator and rotor yoke can be ignored. Under these circumstance, nodes 1–6 in this figure are magnetic equipotential. Both permeance on main path and fringing path are decided by the length, sectional area and permeability, hence the magnetic circuit equation for the two paths are given as

$$\frac{2}{l_{stk} \cdot D_s \cdot \beta_a} \left( \frac{g_m}{\mu_0} + \frac{l_p}{\mu_m} \right) \phi_m = NI, \quad (19)$$

$$\frac{2}{l_{stk} \cdot D_s \cdot (\beta_s - \beta_a)} \left( \frac{g_f}{\mu_0} + \frac{l_p}{\mu_f} \right) \phi_f = NI, \quad (20)$$

where  $\phi_m$  and  $\phi_f$  are the magnetic flux on main path and fringing path;  $l_p$ , the total length of the rotor and stator poles, equals to  $(D_{sy} + D_r - D_s - D_{ry})/2$ ; the iron permeability on these two paths are assumed as  $\mu_m$  and  $\mu_f$ ,  $g_m$  and  $g_f$  are the air gap on the main path and fringing path; the overlapping angle,  $\beta_a$ , is solved by

$$\lambda_s(I, \theta_r) = l_{stk} (A_z(\rho_2, \theta_c) - A_z(\rho_2, 0)) = \sum_{n=\text{odd}} \frac{4N^2 \theta_c \mu_0 l_{stk} I}{(n\pi)^2} \left( \frac{\sin(n\pi\varphi_1/\theta_c)}{\varphi_1} + \frac{\sin(n\pi\varphi_2/\theta_c)}{\varphi_2} \right) \frac{\rho_2^{2n\pi/\theta_c} + \rho_1^{2n\pi/\theta_c}}{\rho_2^{2n\pi/\theta_c} - \rho_1^{-2n\pi/\theta_c}}. \quad (18)$$

$$\beta_a = \begin{cases} \theta_r - \theta_m, & (\theta_r \leq \beta_s + \theta_m) \\ \beta_s, & (\theta_r > \beta_s + \theta_m) \end{cases} \quad (21)$$

With the solving method described in [23],  $\phi_m$  is given as: (see (22))

where  $l_{m1}, l_{m2}$  are solved by

$$l_{m1} = l_p + (u_r + 1)g_m, \quad l_{m2} = l_p - (u_r - 1)g_m, \quad (23)$$

the air gap  $g_m$  is equal to  $D_s/2 - D_r/2$ , and  $B_{sat}$  means the saturation magnetic flux density characterising the iron. The solution of  $\phi_f$  has the similar form with  $\phi_m$ : (see (24))

where  $l_{f1}, l_{f2}$  are solved

$$l_{f1} = l_p + (u_r + 1)g_f, \quad l_{f2} = l_p - (u_r - 1)g_f. \quad (25)$$

Additional,  $g_f$  is the air gap and expressed as

$$g_f(\beta_a) = g_m + \left( \mu_0 N^2 \frac{l_{stk} \cdot D_s \cdot \beta_s}{2L_m} - g_m \right) \left( 1 - \frac{\beta_a}{\beta_s} \right). \quad (26)$$

With the main and fringing magnetic flux  $\phi_m$  and  $\phi_f$  solved, the flux  $\lambda_e$  linked by one SRM phase is the sum of the main flux linkage  $\lambda_m$  and the fringing flux linkage  $\lambda_f$

$$\lambda_e(I, \theta_r) = \underbrace{N \cdot \phi_m}_{\lambda_m} + \underbrace{N \cdot \phi_f}_{\lambda_f}. \quad (27)$$

**2.1.3 Hybrid model:** The HAM can be concluded as

$$\lambda(I, \theta_r) = \begin{cases} \lambda_e(I, \theta_m) + \frac{k_e}{k_s} [\lambda_s(I, \theta_r) - \lambda_s(I, \theta_m)], & 0 \leq \theta_r < \theta_m \\ \lambda_e(I, \theta_r), & \theta_m \leq \theta_r \leq \theta_c \end{cases} \quad (28)$$

where

$$k_e = \frac{\partial \lambda_e(I, \theta_r)}{\partial \theta_r} \Big|_{\theta_r=\theta_m}, \quad k_s = \frac{\partial \lambda_s(I, \theta_r)}{\partial \theta_r} \Big|_{\theta_r=\theta_m}.$$

We keep the solution of the MEC in the overlapping region, and change the solution of space harmonic model in the non-overlapping region to guarantee the continuity of this model. With the integrating method given as (28), the HAM is first-order derivative continuous with respect to  $\theta_r$ , and arbitrary-order derivative continuous with respect to  $I$ . Indeed, this HAM is closer to reality because the effects of magnetic saturation are taken into account in the entire motion region of rotor, which are verified by comparing the solution of the HAM model with the results from the FEM model in the testing.

## 2.2 Modelling the SRM inverter

In the SRM drive system, the IGBT inverter provides the exciting current for each phase of the SRM. As the testing object of this work is the controller, it is not necessary to employ the real

inverter in the HIL simulation. In this work, each phase of the SRM is equivalent to an inductance related to the exciting current and rotor position. Considering the phase inductance as a component in the inverter, the current and the flux linkage on each phase are able to be solved accurately through the circuit simulation method. Each phase of SRM is excited by the IGBT inverter with two IGBTs and two diodes as shown in Fig. 3a. This figure also demonstrates the interface between the controller and motor. The inputs of the controller contain the electromagnetic torque  $T_e$ , rotor angular speed  $\omega_n$ , and mechanical rotation  $\theta$ , while the outputs of the controller, defined as  $s = [s_1, s_2, \dots, s_M]^T$ , are the gate signals for each IGBT inverters. Two IGBTs are controlled synchronously, and their characteristics are described by a switching-function with high or low impedance capability,  $R_{off}$  or  $R_{on}$ , occurs when the control signal  $s$  is turned off or on. The IGBT inverter has three states as shown in Fig. 3b, which can be described as corresponding discrete differential equations through the Backward Euler

$$f(I_n) = \begin{cases} (R_p + R_{off}) \cdot I_n + V_\lambda - V_s, & \text{state a} \\ (R_p + R_{on}) \cdot I_n + V_\lambda - V_s, & \text{state b} \\ R_p \cdot I_n + V_\lambda + V_s + 2 \cdot V_d, & \text{state c} \end{cases} \quad (29)$$

where  $R_p$  is the resistance of the phase coils,  $V_s$  and  $V_d$  represent the power supply voltage and diode voltage drop, and  $V_\lambda$  is the induced voltage of phase coils

$$V_\lambda = \frac{\lambda(I_n, \theta_r) - \lambda(I_h, \theta_r)}{t_s}. \quad (30)$$

With the non-linearity in the HAM, the Newton–Raphson (N–R) method is employed to solve  $I_n$  in the emulation. The iteration process is given in (31), where  $I_{n,k}$  is the result of  $k$ th iteration in the computation process for solving  $I_n$ .

$$I_{n,k+1} = I_{n,k} - f(I_{n,k}) \cdot \left( \frac{df(I)}{dI} \Big|_{I=I_{n,k}} \right)^{-1} \quad (31)$$

## 2.3 Motion equations

The electromagnetic torque is computed by the derivation of the machine coenergy related to the rotor position, and the coenergy is the integration of flux linkage with respect to the current, hence  $T_e$  is

$$T_e(I, \theta) = \sum \int_0^I \frac{\partial \lambda(i, \theta)}{\partial \theta} di. \quad (32)$$

It is hard to obtain the analytical solution of coenergy with a complicated expression of (28). As the HAM is first-order derivative continuous with respect to  $\theta$  and arbitrary-order derivative continuous with respect to  $I$ , Gaussian quadrature is an alternative. The electromagnetic torque is solved below through the three-order Gaussian quadrature, where  $\varpi$  and  $\xi$  mean weight and node, respectively.

$$T_e(I_1, I_2, \dots, I_M, \theta) = \sum_{i=1}^M \sum_{g=0}^2 \frac{I_i \varpi_g}{2} \cdot \frac{\partial \lambda_i(0.5I_i + \xi_g, \theta)}{\partial \theta} \quad (33)$$

$$\phi_m = \mu_0 \cdot N \cdot l_{stk} \frac{D_s \cdot \beta_a}{2g_m} \left[ \left( 1 + \frac{2g_m}{l_p} \right) I + \frac{l_{m1} B_{sat}}{\mu_r \mu_0 N} - \sqrt{\left( \frac{l_{m1} B_{sat}}{\mu_r \mu_0 N} \right)^2 + \frac{2l_{m2} B_{sat}}{\mu_r \mu_0 N} I + I^2} \right], \quad (22)$$

$$\phi_f = \mu_0 \cdot N \cdot l_{stk} \frac{D_s (\beta_s - \beta_a)}{2g_f} \left[ \left( 1 + \frac{2g_f}{l_p} \right) \cdot I + \frac{l_{f1} B_{sat}}{\mu_r \mu_0 N} - \sqrt{\left( \frac{l_{f1} B_{sat}}{\mu_r \mu_0 N} \right)^2 + \frac{2l_{f2} B_{sat}}{\mu_r \mu_0 N} I + I^2} \right], \quad (24)$$

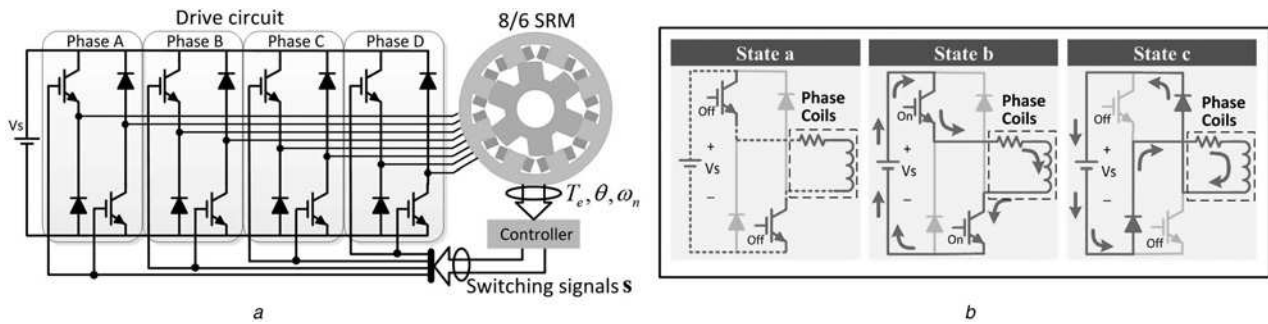


**Fig. 3** SRM drive system  
 a Schematic of the SRM drive  
 b States of IGBT inverter

Thus, the angular speed and position of the rotor are solved in (34) if we assume damping exists in the machine.

$$\omega_n = \omega_h + \frac{T_e - \omega_h \cdot \eta}{J} t_s, \quad \theta_n = \theta_h + \omega_n \cdot t_s. \quad (34)$$

### 3 Real-time hardware emulation SRM drive system on FPGA

#### 3.1 FPGA implementation

The hardware emulation of the SRM drive system on the FPGA is presented in Fig. 4a. The real-time model consists of four main modules: **Circuit Module**, **Phase Flux Linkage Module**, **Motion Module**, and **Control Module**. The first three modules are employed to solve the circuit equation, magnetic flux linkage, motion equation respectively, while the **Control Module** implements the controller with the specific control algorithm. In addition, since the 32-bit single-precision floating-point format (IEEE standard 754) is employed for digital hardware implementation, one component in **Control Module** converts the data format to 16-bit fixed point data for displaying on oscilloscope via DAC interface at the end of each simulation time-step. The **Timer Generator** module is employed to

generate the clock signal for each module, and the trigger signal of each time-step and control cycle. In general, the frequency of 'start\_con' is the integer times of 'start\_sim', because the control period is always lower than the simulation time-step. Represented by different types of arrows, the computational data and control signals exchanged between these modules are depicted in Fig. 4a. In addition, there are a series of 1-bit 'start' and 'done' signals control the emulation flow between each module. The detailed flow of the emulation is depicted by the finite state machine (FSM) in Fig. 4b.

#### 3.2 Exploitation of parallelism

**3.2.1 Parallelism and latency in one time step:** Thanks to the large amount of configurable hardware slices, the FPGA possesses the feature of executing different computation tasks concurrent. In the hardware emulation, we exploit two level of parallelisms are used to reduce the latency in each step:

- (i) Parallelism in topology: the phases of the SRM can be considered as independent with each other.
- (ii) Parallelism in tasks: some components from states  $S_2$  to  $S_6$  in the FSM can be executed concurrently.

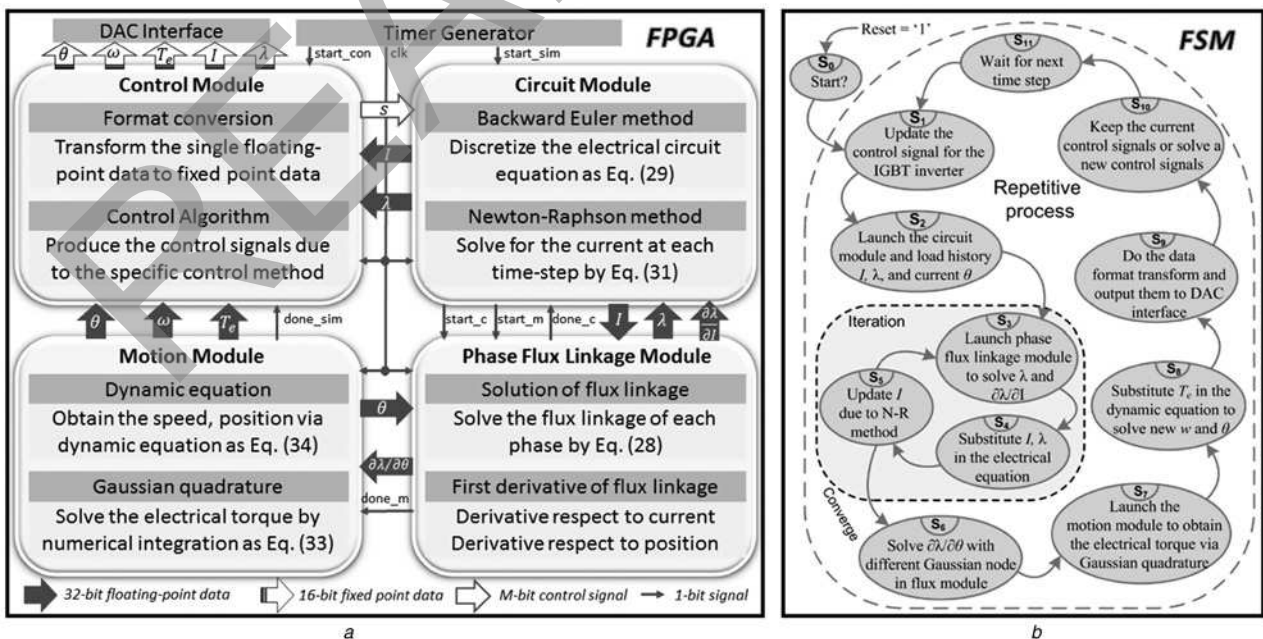


**Fig. 4** Schematic of the FPGA implementation  
 a Hardware emulation of SRM drive system on FPGA  
 b FSM for flow control in the emulation

In Fig. 5a, Steps 1–4 correspond to the states  $S_2 - S_6$  while Step 5 represents the states  $S_7 - S_9$  in the FSM. In the processing, the computation for each phase is independent and all possible parallel calculations are taken into account for the realisation. Excepting the Step 5 implemented in serial mode, both parallelism in topology and tasks exist in the other steps. In this case,  $151 \times K + 190$  clock periods are required for one simulation time-step, where  $K$  means the number of iterations in the N–R method.

**3.2.2 Detailed implementation for flux linkage solution:** To solve the non-linear SRM model described before, floating-point operators and coordinate rotational digital computer algorithm intellectual property (IP) cores which allow a range of floating-point arithmetic operations and fixed point trigonometric functions to be performed on FPGA are necessary. As the universal IP core allow interface with data stream, time-domain-multiplexing (TDM) and pipelined mode are employed to implement these derived equations. The arithmetic of  $\lambda(I_0, \theta_r)$  for solving flux linkage in the Step 1 of Fig. 5a is presented in Fig. 5b, and the other computation can be designed in a similar way.

With the input variables, including the mechanical rotation of rotor  $\theta$  and current  $I$ , there are five parts in Fig. 5a for solving the phase flux linkage  $\lambda$  due to (28) based on the IP cores in this figure. Part I do the modulus operator to obtain the rotor position  $\theta_r$  at the beginning of calculation, then, the rotor position is compared with the threshold  $\theta_m$  via the CP IP core to decide the branches of arithmetic. Meanwhile, in Part II, the derivative of main flux linkage with respect to rotor position  $\partial\lambda_m/\partial\theta$ , which is a part of variable  $k_e$  in (28), can be calculated in parallel with the operator in Part I. Part III implements the equation of (22) and

(24) to solve flux linkage in the overlapping region, while Part IV realises (3), (4) and Part V realises (18), respectively, to obtain the flux linkage in the non-overlapping region.

As the expressions realised by Part II, Part III and Part IV are able to be divided into many independent components which are realised by corresponding IP cores, TDM model is effective to the maintain the computation efficiency and resource of FPGA. To construct a TDM unit, the **Mux** and **Demux** are necessary to select the input and output for the IP core depending on the state of the computation module. On the other hand, the computation components in Part I and Part V are implemented in serial mode. Furthermore, a pipelined processing unit ended with **A2** is designed in Part V to obtain the summation of Fourier series in (18). After that, **A1** and **M2** in Part V are also designed in TDM model for the add and multiply operator in (28).

#### 4 Real-time emulation results and co-simulation validation

We employ three case studies related to the steady-state characteristics and closed-loop control of an 8/6 and a 6/4 SRM. The comparison between the solution from the real-time HIL emulator and the 2D FEM co-simulation highlights the performance of the proposed HAM. The hardware design is targeted to Xilinx<sup>®</sup> Virtex-7 XC7VX485T FPGA with 100 MHz clock frequency shown in Fig. 6a, while the 2D FEM co-simulation model is built in Ansys Maxwell<sup>®</sup>, Ansys Simplorer<sup>®</sup>, and Matlab/Simulink<sup>®</sup> as shown in Fig. 6b. The rated power, voltage, and speed of the two types of SRM are set as 550 W, 110 V, and 1500 rpm respectively in the FEM software, and the design parameters are listed in the Appendix.

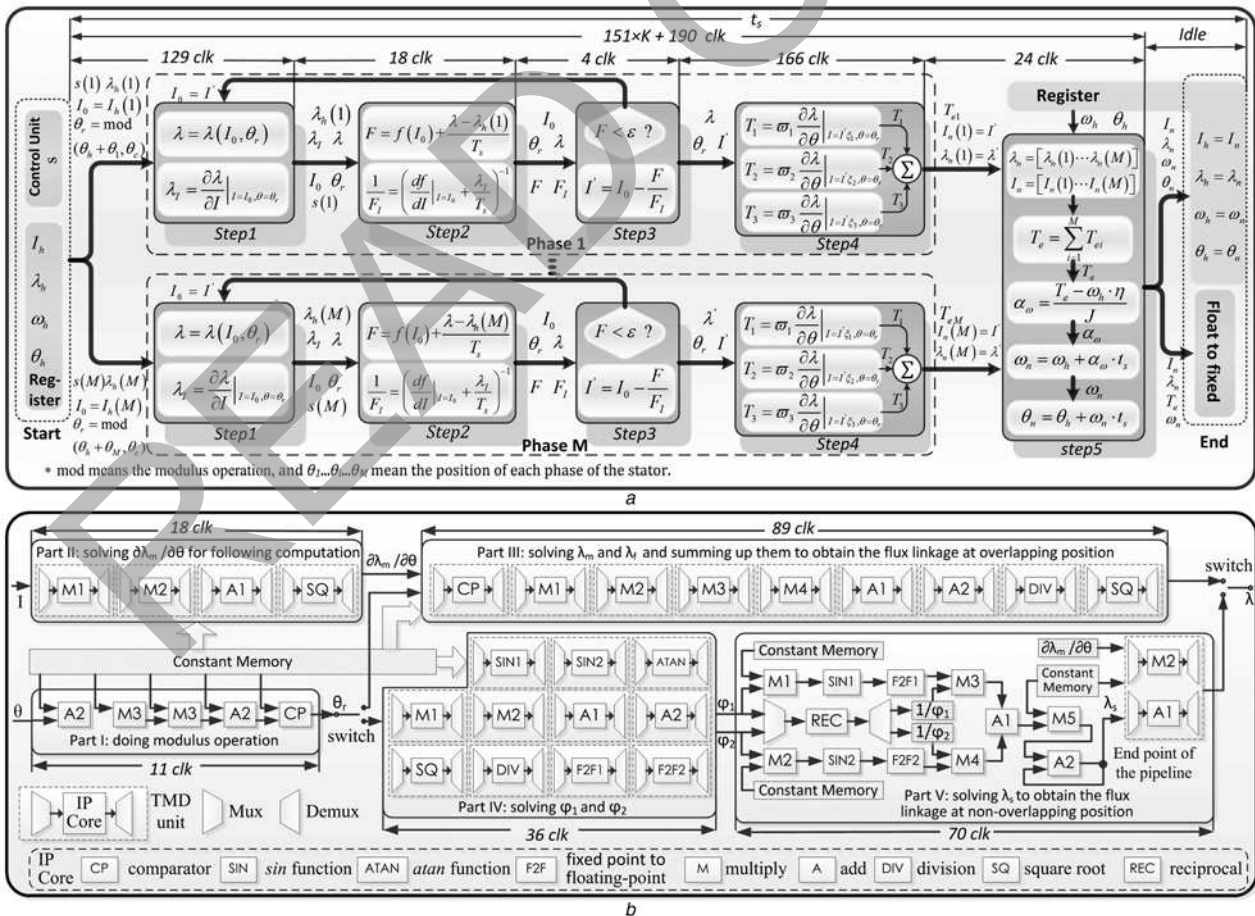


**Fig. 5** Computation unit for the FPGA implementation  
a Parallelism of digital hardware implementation in one time-step  
b Detailed design method to solve phase flux linkage  $\lambda$  in Step 1 of Fig. 5a

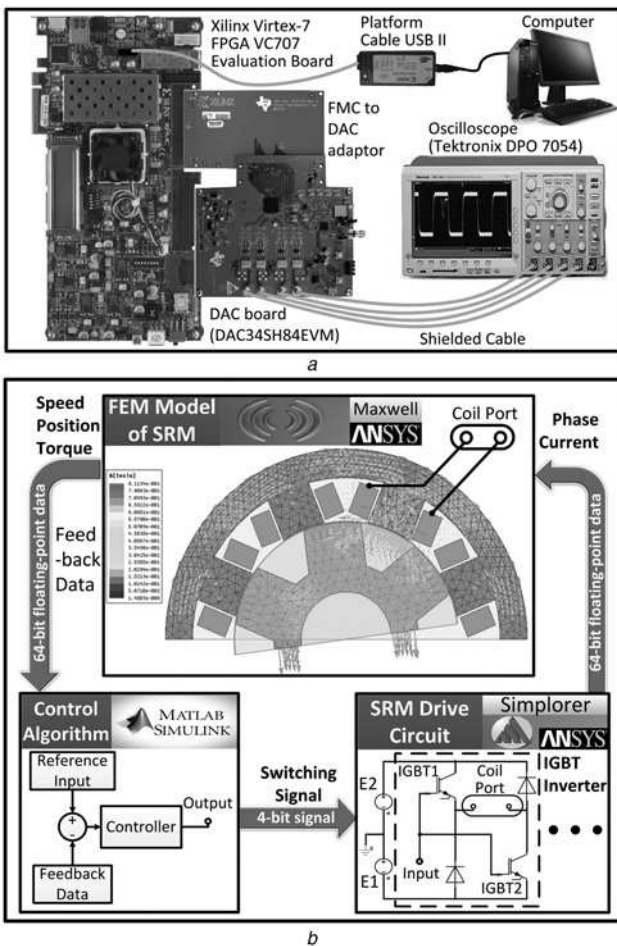


**Fig. 6** Different modelling method for the SRM drive system  
 a FPGA-based real-time emulator  
 b Co-simulation based on FEM

#### 4.1 Steady-state characteristics of SRM

In case I, with four different rated current, 3, 6, 10, and 15 A, the steady-state characteristics of the 8/6 and 6/4 SRM are solved

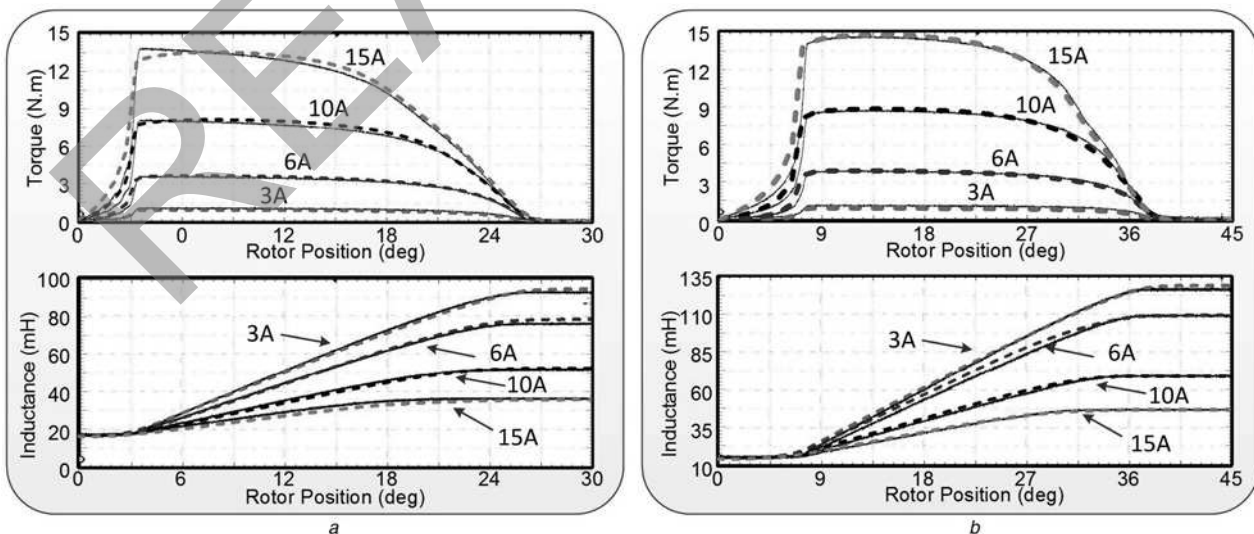


**Fig. 7** Electromagnetic torque and inductance of one phase in SRM with different exciting current versus the rotor position solved by the real-time HAM (solid lines) and the FEM (dashed lines)  
 a 8/6 SRM  
 b 6/4 SRM

when the rotor position locates in the range of  $[0, \theta_c/2]$ . The output torque and inductance computed using the FPGA-based real-time model and the data from FEM software are shown in Fig. 7. To get the real-time solution, we employ the phase flux linkage module in the FPGA design. Since there are four DA channels on the DAC board, four such modules are used for solving the inductance and electromagnetic torque of the same phase with different exciting currents and rotor position. In addition, it is required to verify that the model is pushed sufficiently into saturation region. With magnetic flux divided by the sectional area, the magnetic flux density is solved. At the aligned position, the B-field is equal to 1.78 T when the exciting current is 6 A, which is closed to the value of  $B_{sat}$ . Therefore, we can conclude that the HAM is able to work in the saturation region in the real-time computation.

#### 4.2 Closed-loop control result

The transient performance of the proposed non-linear real-time SRM model is investigated by using two different closed-loop controllers in the HIL simulation. The control object is the turning on and off state of the IGBT inverter. In addition, we assume that the diode voltage drop in the IGBT inverter are equal to 0.7 V, the resistance of each phase coils is  $4.41 \Omega$ , the rated voltage is 110 V, and the damping  $\eta$  is  $0.02 \text{ N} \cdot \text{m} \cdot \text{s}/\text{rad}$ .

**4.2.1 Position feedback control:** In case II, the position of the rotor is employed as the feedback signal. The switch signals for the IGBT inverter and the rotor position meet the relationship

$$s = \begin{cases} 1, & (0 \leq \theta_r \leq \frac{\theta_c}{M}) \\ 0, & (\frac{\theta_c}{M} < \theta_r < \theta_c) \end{cases} \quad (35)$$

In this case, the rotor speed, electromagnetic torque, and flux linkage and current in each phase of the 8/6 SRM are shown in Fig. 8. Fig. 9 are the detailed views of the results of the real-time HIL simulation and co-simulation, respectively, and the curves for the same solution object are superimposed to highlight the similarity between the different solutions. As the performance of the 6/4 SRM looks similar with the 8/6 SRM, the results of the 6/4 SRM are omitted. Furthermore, with the phase current exceeding 20 A, the maximum B-field is approximated to 1.85 T at the start point,

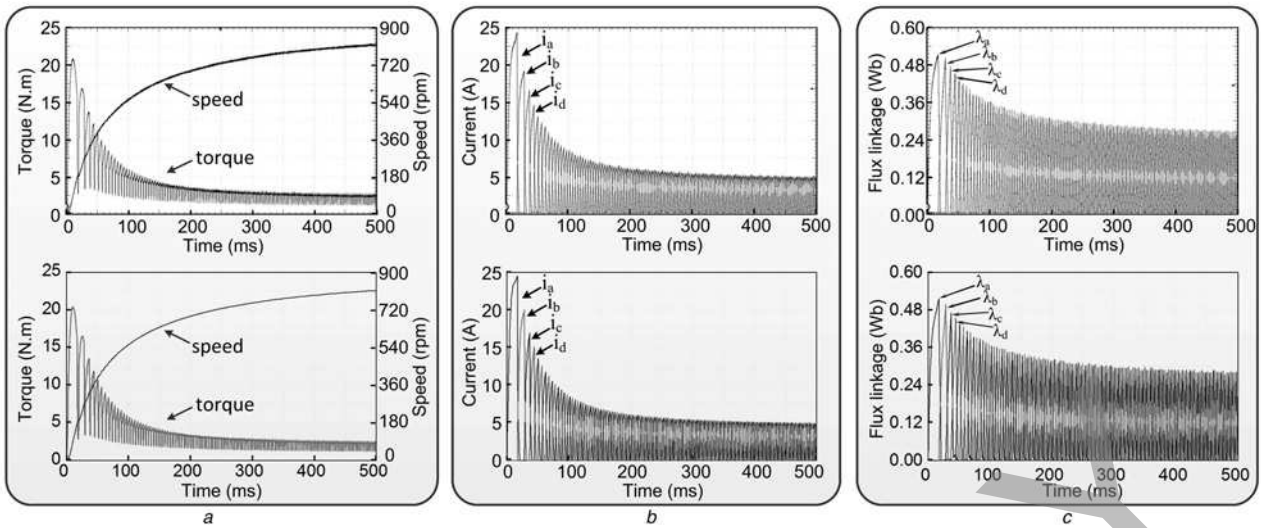


**Fig. 8** Performance of the 8/6 SRM drive system with position feedback control solved by the HIL emulation (top sub-figures) and the off-line co-simulation (bottom sub-figures)

- a Torque and speed
- b Phase currents
- c Phase flux linkages

which implies that the real-time model enters into saturation sufficiently in the HIL simulation.

**4.2.2 Speed feedback control:** To realise speed regulation in case III, a PID controller is employed to calculate the desired torque of SRM using

$$T_{\text{desired}} = G_{\text{PID}}(z) \cdot (w_{\text{desired}} - w_{\text{real}}) + w_{\text{real}} \cdot \eta. \quad (36)$$

In this case, the parameters of PID controller are:  $K_P = 0.84$ ,  $K_I = 0.84$ ,  $K_D = 0.02$ . The desired torque is distributed to each phase through a contour function, so that the required output torque of phase  $i$  is

$$T_i = T_{\text{desired}} \cdot [\text{Sgn}(T_{\text{desired}}) \cdot f_{c+}(\theta_r) + \text{Sgn}(-T_{\text{desired}}) \cdot f_{c-}(\theta_r)]. \quad (37)$$

$\text{Sgn}()$  is a mathematical function that extracts the sign of a real number and  $f_{c+}(\theta_r)$ ,  $f_{c-}(\theta_r)$  are the contour function defined in one cycle of rotor position as

$$f_{c+}(\theta_r) = \begin{cases} \frac{2 \cdot M}{\theta_c} \cdot \theta_r, & \left(0 \leq \theta_r < \frac{\theta_c}{2 \cdot M}\right) \\ 1, & \left(\frac{\theta_c}{2 \cdot M} \leq \theta_r < \frac{\theta_c}{M}\right) \\ 3 - \frac{2 \cdot M}{\theta_c} \cdot \theta_r, & \left(\frac{\theta_c}{M} \leq \theta_r < \frac{3 \cdot \theta_c}{2 \cdot M}\right) \\ 0, & \left(\frac{3 \cdot \theta_c}{2 \cdot M} \leq \theta_r < \theta_c\right) \end{cases}. \quad (38)$$

$f_{c+}(\theta_r)$  and  $f_{c-}(\theta_r)$  are odd symmetry respecting to the axis of  $\theta_r = \theta_c/2$ . When the desired output torque of the corresponding phase exceed a constant, the switch of the IGBT inverter will turn

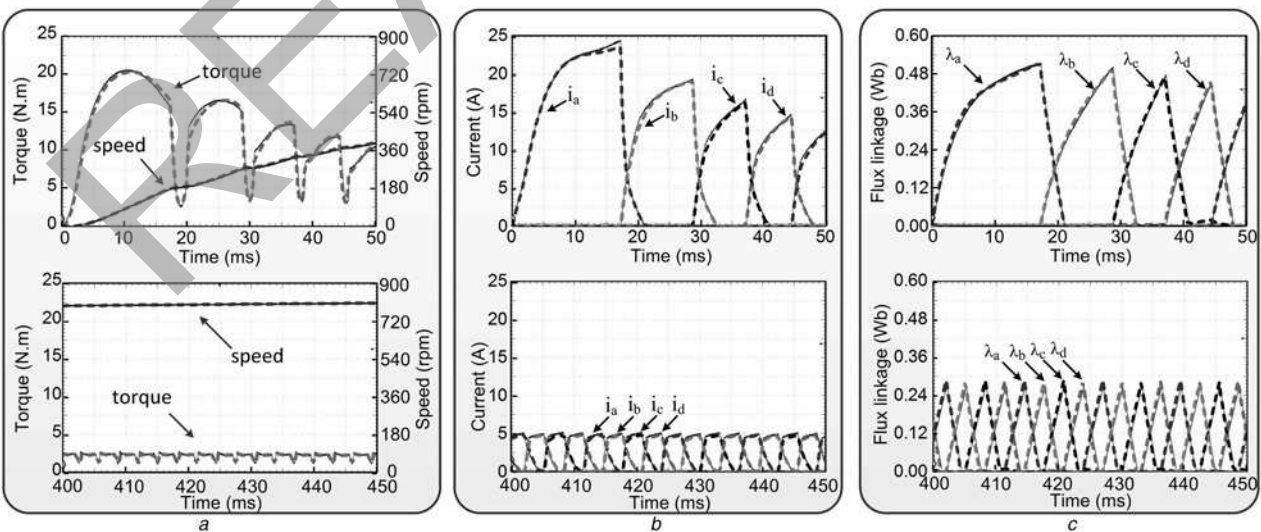


**Fig. 9** Detailed views of the curves in Fig. 8 with the results of real-time HIL emulation (solid line) and co-simulation (dashed line) superimposed

- a Torque and speed
- b Phase currents
- c Phase flux linkages

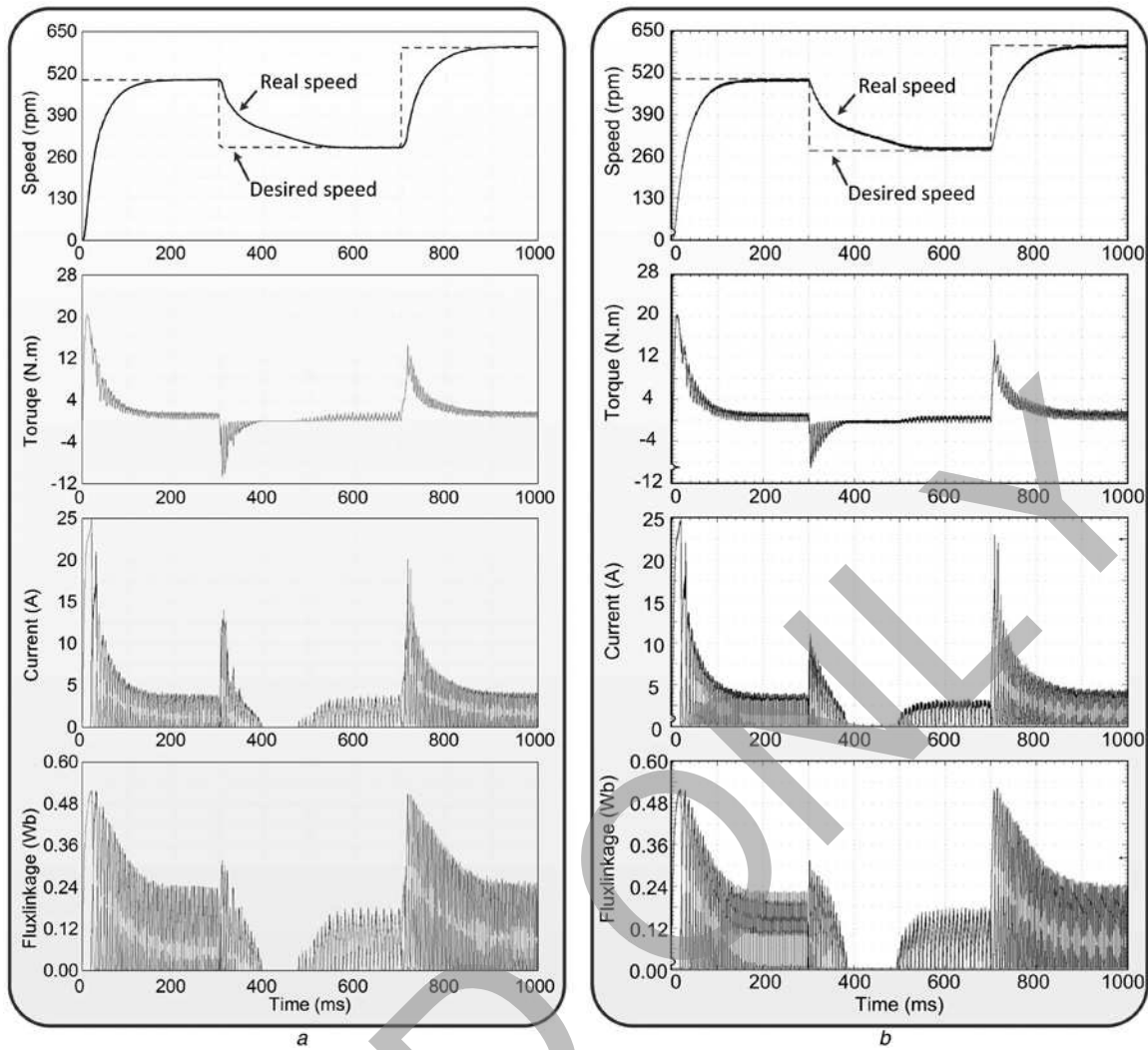


**Fig. 10** Speed, electromagnetic torque, phase current and phase flux linkage of the 8/6 SRM with speed feedback control

a Off-line co-simulation  
b Real-time HIL emulation

on. In this emulation, we set the constant as  $0.5 \text{ N} \cdot \text{m}$ . Moreover employing the results from the off-line co-simulation for comparison, the desired and real speed of rotor, electromagnetic torque, phase currents and phase flux linkage of 8/6 SRM solved by the HIL simulation are shown in Fig. 10, and the result of the 6/4 SRM are omitted.

### 4.3 Latency analysis

Since the real-time hardware emulation is realised by 100 MHz FPGA clock frequency, the period of 'clk' is equal to 10 ns in Fig. 5. Thus, the detailed execution time of each state for the HIL simulation can be known. The time-step of the FPGA-based real-time model,  $t_s$ , is equal to  $5 \mu\text{s}$ . As  $K$  is always equal to 2 to obtain the convergent result in the N-R method, the execution time is equal to  $4.92 \mu\text{s}$  and the idle time is  $0.08 \mu\text{s}$ .

**Table 1** Relative deviation of the steady-state characteristics in Case I

Relative deviation		$I = 3 \text{ A}, \%$	$I = 6 \text{ A}, \%$	$I = 10 \text{ A}, \%$	$I = 15 \text{ A}, \%$
8/6 SRM	$\Delta T_e$	3.99	4.29	5.03	5.29
	$\Delta L$	1.81	1.49	1.83	2.49
6/4 SRM	$\Delta T_e$	4.37	4.65	5.43	6.10
	$\Delta L$	2.90	4.29	3.98	3.24

The co-simulation was executed on Intel<sup>®</sup> Xeon<sup>®</sup> E5-2609 CPU with 8 cores, 2.4 GHz, 32 GB, platform running Windows<sup>®</sup> 7 operating system. The time-step of the co-simulation was set to  $100 \mu\text{s}$  and the meshing method employed the default parameters. Under these circumstance, the co-simulation costs more than five hours to run an 1s simulation. Therefore, the FPGA-based real-time non-linear HAM realised a significant improvement in the computational efficiency.

### 4.4 Accuracy analysis

In the case I, we calculate the average relative deviation of inductance and torque between the FEM software and real-time HAM at 60 sampling points whose rotor positions are distributed from 0 to  $\theta_c/2$  uniformly as

$$\Delta T_e = \frac{\sum_{i=1}^{60} |T_{i,\text{HAM}} - T_{i,\text{FEM}}|}{\sum_{i=1}^{60} T_{i,\text{FEM}}}, \quad (39)$$

$$\Delta L = \frac{1}{60} \sum_{i=1}^{60} \frac{|L_{i,\text{HAM}} - L_{i,\text{FEM}}|}{L_{i,\text{FEM}}}, \quad (40)$$

and show the results in Table 1.  $T_{i,\text{HAM}}$ ,  $T_{i,\text{FEM}}$ ,  $L_{i,\text{HAM}}$ ,  $L_{i,\text{FEM}}$  are the torque and inductance solved by the HAM and FEM software

**Table 2** Relative deviation in Closed-loop control testing

Relative deviation		$\Delta\omega, \%$	$\Delta T_e, \%$	$\Delta \sum_{i=1}^M I_i, \%$	$\Delta \sum_{i=1}^M \lambda_i, \%$
8/6	Case II	2.94	4.89	4.78	3.72
SRM	Case III	0.71	5.64	5.89	6.53
6/4	Case II	3.16	4.92	5.31	4.06
SRM	Case III	0.94	4.23	6.09	6.82

respectively. The average of torque is used as denominator for calculation because the torque solutions at some sampling points approximate to zero which may result in a huge relative deviation.

In the case II and case III, 1000 sampling points of co-simulation are chosen uniformly in the travel range to calculate the relative deviation. Since the rotor positions in the solution of the HIL emulator are not exactly the same with the co-simulation, interpolation method is employed to process the results from HIL emulation so that the rotor position in these two sets of data are identical. The expression to calculate the average relative deviation are given as follows and the results are shown in Table 2.

$$\Delta D = \frac{1}{1000} \sum_{i=1}^{1000} \left| \frac{D_{i,HIL} - D_{i,CoSim}}{D_{i,CoSim}} \right|. \quad (41)$$

Different subscripts represent the solution from HIL emulation and co-simulation respectively, and  $D$  represents different variables:  $\omega$ ,  $T_e$ ,  $\sum_{i=1}^M I_i$ , and  $\sum_{i=1}^M \lambda_i$ . The sum of phase current and phase flux linkage are used as the evaluation targets in cases II and III, so that we can avoid the denominator becomes zero when the some IGBT inverters turn off.

With the relative deviation shown in Tables 1 and 2, the HIL emulator shows the satisfactory agreement with the co-simulator which employs the FEM model. The real-time model reflects the characteristics of real machine well and meets the requirements for controller testing in HIL scenarios.

## 5 Conclusion

SRM is gaining increasing popularity in various industrial application, and as such requiring accurate and efficient real-time models for HIL simulation. A non-linear HAM taking advantage of the SHM and MEC method to calculate the flux linked by each phase of SRM is proposed for real-time HIL emulation. This model is realised on the FPGA, and several tests, including steady-state characteristics computation and closed-loop control, are undertaken to evaluate the performance. In the HIL emulation, the real-time model is realised at a  $5 \mu\text{s}$  time-step with 100 MHz clock frequency. The co-simulation based on Ansys Maxwell<sup>®</sup>, Ansys Simplorer<sup>®</sup>, and Matlab/Simulink<sup>®</sup> is used as comparison to verify the computational accuracy. The results show that the HAM achieves sufficient accuracy for the HIL simulation of SRM drive system. Indeed, because the proposed HAM is a 2D model, the end effects are ignored, which may result in the error of the HIL simulation especially in the SRM whose diameter is much larger than length; thus, building 3D hybrid model to analyse the SRM drive system is planned for future research.

## 6 References

- Ding, W., Liu, L., Lou, J., *et al.*: 'Design and control of a high-speed switched reluctance machine with conical magnetic bearings for aircraft application', *IET Electr. Power Appl.*, 2013, 7, (3), pp. 179–190
- Ruba, M., Viorel, I.A., Szabo, L.: 'Modular stator switched reluctance motor for fault tolerant drive systems', *IET Electr. Power Appl.*, 2013, 7, (3), pp. 159–169

- Nezamabadi, M.M., Afjei, E.: 'Switched reluctance motor for hybrid motion control: design, modelling, and sensorless drive', *IET Electr. Power Appl.*, 2016, 10, (6), pp. 498–507
- Wang, H., Wang, Y., Liu, X., *et al.*: 'Design of novel bearingless switched reluctance motor', *IET Electr. Power Appl.*, 2012, 6, (2), pp. 73–81
- Cheng, H., Chen, H., Yang, Z.: 'Average torque control of switched reluctance machine drives for electric vehicles', *IET Electr. Power Appl.*, 2015, 9, (7), pp. 459–468
- Cheng, H., Chen, H., Yang, Z.: 'Design indicators and structure optimisation of switched reluctance machine for electric vehicles', *IET Electr. Power Appl.*, 2015, 9, (4), pp. 319–331
- Cebi, A., Guvenc, L., Demirci, M., *et al.*: 'A low cost, portable engine electronic control unit hardware-in-the-loop test system' Proc. IEEE Int. Symp. on Industrial Electronics, Croatia, 2005, pp. 293–298
- Dufour, C., Cense, S., Belanger, J.: 'FPGA-based switched reluctance motor drive and DC-DC converter models for high-bandwidth HIL real-time simulator'. Proc. 15th Eur. Conf. Power Electron. Appl. (EPE), Lille, France, September 2013, pp. 1–8
- Wang, Q., Chen, H., Xu, T., *et al.*: 'Inductance estimation method for linear switched reluctance machines considering iron losses', *IET Electr. Power Appl.*, 2016, 10, (3), pp. 181–188
- Fahimi, B., Suresh, G., Mahdavi, J., *et al.*: 'A new approach to model switched reluctance motor drive application to dynamic performance prediction, control and design'. Proc. IEEE Power Electronics Specification Conf., Fukuoka, Japan, May 1998, pp. 2097–2102
- Chi, H.P., Lin, R.L., Chen, J.F.: 'Simplified flux-linkage model for switched-reluctance motors', *IEEE Proc. Electr. Power Appl.*, 2005, 152, (3), pp. 577–583
- Xia, C.L., Xue, M., Shi, T.N.: 'A new rapid nonlinear simulation method for switched reluctance motors', *IEEE Trans. Energy Convers.*, 2009, 24, (3), pp. 284–290
- Zhong, R., Xu, Y., Cao, Y., *et al.*: 'Accurate model of switched reluctance motor based on indirect measurement method and least square support vector machine', *IET Electr. Power Appl.*, 2016, 10, (9), pp. 916–922
- Andrade, D.A., Krishnan, R.: 'Characterization of switched reluctance machines using Fourier series approach'. Proc. 36th IEEE Ind. Applications Annual Meeting, Chicago, USA, September 2001, pp. 48–54
- Ohdaehi, Y.: 'Optimum design of switched reluctance motors using dynamic finite element analysis', *IEEE Trans. Magn.*, 1997, 33, (2), pp. 2033–2036
- Garcia-Amoros, J., Molina, B.B., Andrada, P.: 'Modelling and simulation of a linear switched reluctance force actuator', *IET Electr. Power Appl.*, 2013, 7, (5), pp. 350–359
- Parreira, B., Rafael, S., Pires, A.J., *et al.*: 'Obtaining the magnetic characteristics of an 8/6 switched reluctance machine: from FEM analysis to the experimental tests', *IEEE Trans. Ind. Electron.*, 2005, 52, (6), pp. 1635–1643
- Radun, A.V.: 'Analytical calculation of the switched reluctance motor's unaligned inductance', *IEEE Trans. Magn.*, 1999, 35, (6), pp. 4473–4481
- Liu, C.T., Kuo, J.L., Chen, L.F., *et al.*: 'Interaction force analysis of transverse flux linear switched reluctance machine by Fourier projection method', *IEEE Trans. Energy Convers.*, 1996, 11, (6), pp. 62–69
- Lubin, T., Mezani, S., Rezzoug, A.: 'Exact analytical method for magnetic field computation in the air gap of cylindrical electrical machines considering slotting effects', *IEEE Trans. Magn.*, 2010, 46, (4), pp. 1092–1099
- Krishnan, R.: 'Switched reluctance motor drives: modeling, simulation, analysis, design, and applications' (CRC Press, 2001)
- Ding, W., Yin, Z., Liu, L., *et al.*: 'Magnetic circuit model and finite-element analysis of a modular switched reluctance machine with E-core stators and multi-layer common rotors', *IET Electr. Power Appl.*, 2014, 8, (8), pp. 296–309
- Radun, A.V.: 'Analytically computing the flux linked by a switched reluctance motor phase when the stator and rotor poles overlap', *IEEE Trans. Magn.*, 36, (4), pp. 1996–2003
- Duman, E., Can, H., Akin, E.: 'Real time FPGA implementation of induction machine model – a novel approach', Proc. Int. ACEMP, Bodrum, 2007, pp. 603–606
- Zanuso, G., Peretti, L., Zigliotto, M.: 'Permanent magnet synchronous machines flux linkage estimation with zero steady-state error and its field-programmable gate array implementation', *IET Electr. Power Appl.*, 2015, 9, (4), pp. 332–343

## 7 Appendix

The design parameters of 8/6 and 6/4 SRM used for testing are given as follows: outer diameter of SRM: 120 mm; diameter of the rotor shaft: 30 mm;  $D_r = 76$  mm;  $D_s = 75$  mm;  $D_{ry} = 102$  mm;  $D_{sy} = 48$  mm;  $l_{stk} = 65$  mm;  $N = 142$ ;  $J = 0.014 \text{ kg} \cdot \text{m}^2$ ;  $\mu_0 = 4\pi \times 10^{-7}$ ;  $\mu_r = 5000$ ;  $B_{sat} = 1.8 \text{ T}$ ;  $R_{off} = 2 \text{ M}\Omega$ ;  $R_{on} = 0.1 \Omega$ . The phase number, stator pole radian, and rotor pole radian of the 8/6 SRM are  $M = 4$ ,  $\beta_s = \pi/8$ ,  $\beta_r = \pi/6$  respectively. The phase number, stator pole radian, and rotor pole radian of the 6/4 SRM are  $M = 3$ ,  $\beta_s = \pi/6$ ,  $\beta_r = \pi/4$  respectively.